JBIC Journal of Biological Inorganic Chemistry (2022) 27:573–582
https://doi.org/10.1007/s00775-022-01953-4

ORIGINAL PAPER

Determination of the iron(IV) local spin states of the Q intermediate of soluble methane monooxygenase by Kβ X-ray emission spectroscopy

George E. Cutsail III[1,2] · Rahul Banerjee[3] · Derek B. Rice[1] · Olivia McCubbin Stepanic[1] · John D. Lipscomb[3] · Serena DeBeer[1]

Received: 13 April 2022 / Accepted: 7 August 2022 / Published online: 21 August 2022

Abstract

Soluble methane monooxygenase (sMMO) facilitates the conversion of methane to methanol at a non-heme Fe^{IV}_2 intermediate $MMOH_Q$, which is formed in the active site of the sMMO hydroxylase component (MMOH) during the catalytic cycle. Other biological systems also employ high-valent Fe^{IV} sites in catalysis; however, $MMOH_Q$ is unique as Nature's only identified Fe^{IV}_2 intermediate. Previous ^{57}Fe Mössbauer spectroscopic studies have shown that $MMOH_Q$ employs antiferromagnetic coupling of the two Fe^{IV} sites to yield a diamagnetic cluster. Unfortunately, this lack of net spin prevents the determination of the local spin state (S_{loc}) of each of the irons by most spectroscopic techniques. Here, we use Fe Kβ X-ray emission spectroscopy (XES) to characterize the local spin states of the key intermediates of the sMMO catalytic cycle, including $MMOH_Q$ trapped by rapid-freeze-quench techniques. A pure XES spectrum of $MMOH_Q$ is obtained by subtraction of the contributions from other reaction cycle intermediates with the aid of Mössbauer quantification. Comparisons of the $MMOH_Q$ spectrum with those of known $S_{loc} = 1$ and $S_{loc} = 2$ Fe^{IV} sites in chemical and biological models reveal that $MMOH_Q$ possesses $S_{loc} = 2$ iron sites. This experimental determination of the local spin state will help guide future computational and mechanistic studies of sMMO catalysis.

Graphical abstract

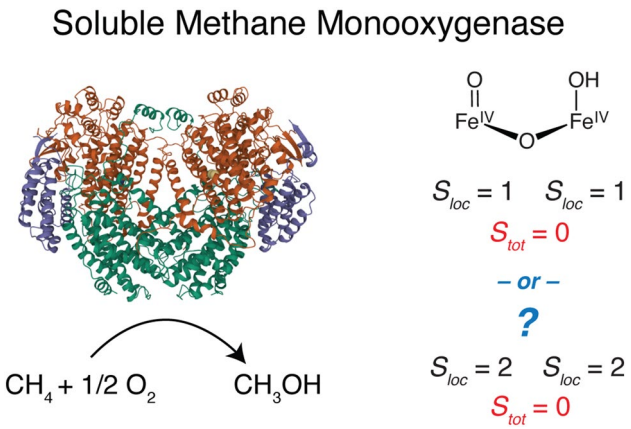

Keywords Methane monooxygenase · Non-heme iron · Spin state · X-ray emission spectroscopy · Rapid freeze-quench

✉ George E. Cutsail III
george.cutsail@cec.mpg.de

✉ Serena DeBeer
serena.debeer@cec.mpg.de

Extended author information available on the last page of the article

Introduction

The conversion of methane to methanol is of significant interest for technologies aimed at gas-to-liquid fuel conversion, and for the sequestration of a greenhouse gas, alongside the desire to understand the fundamental chemistry of strong C–H bond activation. Nature facilitates this challenging chemical reaction with two different methane monooxygenase enzymes [1]. The most common type is the copper-containing particulate methane monooxygenase (pMMO) [2–4], which is a topic of intense research, in particular for the assignment of the active site and its structure [5–11]. In copper limited environments [2, 12], methanotrophic bacteria express the iron-containing soluble methane monooxygenase (sMMO), which has a well characterized non-heme carboxylate-bridged di-iron active site [13, 14].

The active site of sMMO is located within the hydroxylase protein (MMOH) and forms various catalytic intermediates that have been spectroscopically identified [13, 15–25]. An abbreviated catalytic mechanism of MMOH is shown in Fig. 1. For the critical intermediate of interest, $MMOH_Q$, the O–O bond of the preceding peroxo intermediate ($MMOH_P$) has been cleaved and the resultant intermediate is able to activate the strong 105 kcal/mol C–H bond of methane, allowing for its subsequent conversion to methanol. To our knowledge, $MMOH_Q$ is the only di-iron(IV) intermediate that has been identified in Nature [17, 19, 20].

The exact geometric structure of the $MMOH_Q$ intermediate has been hotly debated for over two decades [14, 17, 18, 21, 23–27]. Spectroscopic characterizations of $MMOH_Q$ have included vibrational studies (transient resonant Raman and nuclear resonance vibrational scattering, NRVS), which have also been used to argue for a "closed-core" bis-μ-oxo structure [21, 25]. However, high-resolution Fe K-edge X-ray absorption (HERFD XAS) characterization and pre-edge analysis of $MMOH_Q$ in comparison with biomimetic models support an "open core" structure [23]. Recent HERFD extended X-ray absorption fine structure (EXAFS) measurements of RFQ samples of sMMO were fit with a long Fe–Fe distance of ~ 3.3 Å and showed no evidence for the initially reported 2.46 Å di-iron distance that would have supported a closed-core structure [24]. The short Fe–Fe distance in the previous 1997 EXAFS report [18] was shown to arise from metallic iron background scattering contributions, which are suppressed in the HERFD EXAFS [24]. Because the RFQ samples in the HERFD EXAFS study contained primarily $MMOH_Q$ (~ 50%) and $MMOH_{red}$ (40%), the fitted distance is weighted average of these contributions. As the di-iron distance in $MMOH_{red}$ is established to be ~ 3.2 Å [28], the longer fitted distance of the RFQ samples therefore suggests a longer di-iron distance for $MMOH_Q$ of ~ 3.4 Å, consistent with an open core structure [24]. Further, a recent quantum mechanics-molecular mechanics (QM/MM) computational study of $MMOH_Q$ has shown that the computed spectroscopic signatures of an open core structure are consistent with the Mössbauer, Fe HERFD pre-edge XAS, EXAFS di-iron distance measurements, and resonance Raman [29]. These QM/MM computational studies, however, have not yet been extended to the recently reported NRVS spectrum of $MMOH_Q$ [25].

While the geometric structure of $MMOH_Q$ remains controversial, its electronic structure is also key to understanding catalytic activity and predicting spectroscopic signatures. The initial spectroscopic characterization and identification of $MMOH_Q$ included its characteristic optical absorption at 430 nm and a single observed Mössbauer quadruple doublet in the case of $MMOH_Q$ trapped using the enzyme from *Methylosinus trichosporium* OB3b [16, 19, 20]. The single Mössbauer doublet from two irons was interpreted to indicate that the iron sites have similar coordination environments, thereby yielding overlapping doublets. The isomer shift of the observed doublet is entirely consistent with Fe^{IV} oxidation state, however, the Mössbauer characterization of $MMOH_Q$ remains inconclusive for the assigned local spin states of the iron sites. Low temperature and applied magnetic field Mössbauer spectroscopy of $MMOH_Q$ determined that the total ground spin state of the cluster is $S_{tot} = 0$, meaning that the Fe^{IV} ions are antiferromagnetically coupled, where iron sites must have local spin states (S_{loc}) of intermediate-spin ($S_{loc} = 1$) or high-spin ($S_{loc} = 2$) [20]. As originally stated by Münck, the isomer shift and quadrupole splittings of $MMOH_Q$ are consistent with both $S_{loc} = 1$ and $S_{loc} = 2$ local spin states; the applied field measurement

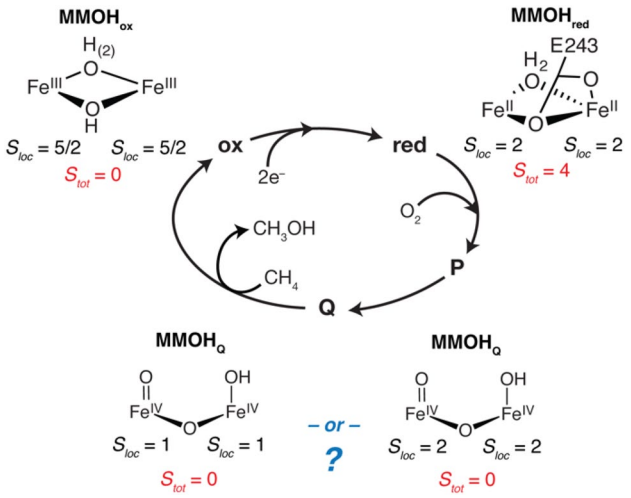

Fig. 1 Abbreviated catalytic scheme of sMMO with corresponding iron oxidation states, local spin states (S_{loc}) and cluster ground spin state (S_{tot}) for $MMOH_{ox}$, $MMOH_{red}$, and $MMOH_Q$. The structure of $MMOH_Q$ is drawn as the proposed 'open-core' structure [23, 24], although a closed $Fe_2(\mu\text{-}O)_2$ core is also proposed [21, 26]

only serves to measure the coupling strength between the two sites [20]. Non-diamagnetic cluster spin states allow for clear local spin-state assignments by Mössbauer spectroscopy. For other mononuclear Fe^{IV} synthetic chemical and biological centers, applied field Mössbauer measurement has been essential to differentiate between intermediate and high-spin iron [30–34]. For example, in the case of the $S_{tot} = 1/2$ Fe^{III}–Fe^{IV} cluster intermediate (X) of ribonucleotide reductase (RNR) [35], the paramagnetic nature of the cluster allowed iron hyperfine and local spin states to be determined by applied field measurements.

Attempts to understand or model both the local and cluster spin states of $MMOH_Q$ through biomimetic chemistry have also been challenging [33, 36–39]. Different local and cluster spin states have been identified in these models, including those with $S_{loc} = 1$ or 2 and ferro- or antiferromagnetic coupling of the iron sites. A sampling of both mono and di-nuclear biomimetic models and their Mössbauer parameters are listed in Table 1. The observed Mössbauer isomer shifts and quadrupole splittings for both $S_{loc} = 1$ and 2 Fe^{IV} sites span a fairly wide range around what is observed for $MMOH_Q$, making a direct assignment of a local spin state from these parameters alone prohibitive.

Perhaps the primary support for the now more commonly accepted $S_{loc} = 2$ spin state of $MMOH_Q$ arises in part from analogy to other non-heme iron chemistry [39]. Enzymatic non-heme Fe^{IV} sites favor local high-spin states, in part due to their weak-field ligand environments [30], similar to that present in MMOH. Furthermore, the enhanced reactivity of high-spin $S = 2$ Fe^{IV} sites to perform hydrogen atom transfer reactions, as seen in other forms of non-heme biological catalysis and biomimetic chemistry [31, 33, 34, 38, 48, 49], is often used to infer a spin-state assignment for $MMOH_Q$. Cryo-reduction experiments of $MMOH_Q$ have also revealed an electronic structure similar in character to RNR-X, suggesting locally high-spin Fe^{IV} sites [50]. Previous computational studies of $MMOH_Q$ also favor $S_{loc} = 2$ iron spin states [29, 51–53]. Ultimately, these chemical analogies or other studies have fallen short of a direct experimental characterization of the local spin states in $MMOH_Q$, motivating an investigation of the electronic structure by means of an alternative spectroscopic approach.

For 3d transition metals, Kβ ($3p \rightarrow 1s$) X-ray emission spectroscopy (XES) has been well demonstrated to be excellent reporter of electronic structure due to 3p–3d exchange in the final state [54–58]. Kβ mainlines have previously been demonstrated to both report and correlate to oxidation state and spin state. As a marker of oxidation state, the maximum of the Kβ mainline, the $K\beta_{1,3}$ feature, generally shifts to higher energy with increased oxidation-state [54]. On the other hand, the intensity of the Kβ' feature, at lower energy, correlates with the number of unpaired electrons, thereby allowing for spin-state assignments. For instance, for ferrous complexes, the presence or absence of the Kβ' has been used as a marker of high-spin ($S = 2$) or low-spin ($S = 0$) electronic configurations [57–60].

Table 1 Mössbauer parameters of various Fe^{IV} sites

	S_{loc}	S_{tot}	δ (mm/s)	ΔE_Q (mm/s)	References
$MMOH_Q$		0	0.17	0.53	[20]
TauD J	2	2	0.31	− 0.88	[40]
RnR X (Fe^{III}-**Fe^{IV}**) [a]	5/2, 2	1/2	0.26	− 0.6	[35]
[L(OH)Fe-(μ-O)**Fe(O)**L]$^{3+}$; L = TPA* [a,b]	1, 1	0	− 0.03	+0.92	[41]
[L**(OH)Fe**-(μ-O)Fe(O)L]$^{3+}$; L = TPA* [a,b]	1, 1	0	0.0	+1.96	[41]
$[Fe^{IV}_2(\mu\text{-}O)_2(TPA^*)_2]^{4+}$	1, 1	0	− 0.04	2.09	[36]
$[(O)(L)Fe^{IV}\text{–}O\text{–}Fe^{IV}(O)(L)]^{2+}$; L = TPA* [b]	2, 2	0	0.14	0.52	[39]
$[(O)(L)Fe^{IV}\text{–}O\text{–}Fe^{IV}(O)(L)]^{2+}$; L = TPA* [b]	1, 2	3	− 0.02, 0.14	− 1.17, 0.82	[39]
$[(TMC)Fe(O)NCMe]^{2+}$ [c]	1	1	0.17	+1.24	[42]
$[(N4Py)Fe(O)]^{2+}$ [d]	1	1	− 0.04	0.93	[43]
$[Fe^{IV}(O)(2PyN2Q)]^{2+}$ [e]	1	1	0.03	0.56	[44]
$[Fe^{IV}(O)(TMG_3tren)]^{2+}$ [f]	2	2	0.24	− 0.29	[45]
$[Fe^{IV}(O)(t\text{Bu}_3TACN)]^{2+}$ [g]	2	2	0.11	+0.96	[46]
Aqueous Fe^{IV} = O	2	2	0.38	− 0.33	[47]

[a] In the case of asymmetric di-iron cluster, the parameters are detailed for the iron in bold

[b] TPA* = tris(4-methoxy-3,5-dimethylpyridyl-2-methyl)amine

[c] TMC = 1,4,8,11-tetramethyl-1,4,8,11-tetraazacyclotetradecane

[d] N4Py = *N*,*N*-bis(2-pyridylmethyl)bis(2pyridyl)methylamine

[e] 2PyN2Q = 1,1-di(pyridin-2-yl)-*N*,*N*-bis(quinolin-2-ylmethyl)methanamine)

[f] TMG_3tren = tris[2-{N-tetramethylguanidyl}ethyl]amine]

[g] $t\text{Bu}_3TACN$ = 1,4,7-tri-tert-butyl-1,4,7-triazacyclononane

While these rule-of-thumb trends may hold true in idealized systematic studies, covalency is shown to have profound influences on the shape and energies of Kβ mainlines [56, 58]. Increasing metal–ligand covalency delocalizes metal 3d orbital character onto the ligands and thus decreases the metal 3p-3d exchange integrals, which determine the final state splitting in Kβ spectra [56]. Ultimately, this relationship predicts that expected shifts of the $K\beta_{1,3}$ to higher energy with increased oxidation-state may be counteracted by increased metal–ligand covalency, making some interpretations across an oxidation state series difficult. However, these challenges generally do not hinder the ability of Kβ XES to probe local spin states and distinguish between spin states in samples of known oxidation-state and similar covalency [54, 56–58, 61, 62]. Generally, Fe Kβ XES is not sensitive to the magnetic spin coupling (J) between the iron centers in bimetallic or larger clusters; therefore, the bulk XES measurement reports on the average local spin state of all iron sites [63–66]. This makes the approach attractive to possibly probe the local spin states in diamagnetic clusters such as $MMOH_Q$ and distinguish between its local spin-state assignments.

Experimental

The sMMO proteins ^{57}Fe-enriched MMOH and MMOB were purified according to protocols described recently in the literature [22, 67]. The Fe Kβ mainline XES spectra were collected on frozen solution samples of $MMOH_{red}$, $MMOH_{ox}$ and freeze-quenched samples (MMOH-RFQ) to trap $MMOH_Q$ of the same samples described in a previously published HERFD EXAFS study [24]. The MMOH-RFQ samples were prepared as previously described by freezing the reaction mixture in precooled sample cell of supercooled liquid nitrogen (-199 °C) [24].

^{57}Fe Mössbauer spectroscopy was used to quantitate the three components, $MMOH_{red}$, $MMOH_{ox}$ and $MMOH_Q$, in the MMOH-RFQ sample. As previously reported [24], the frozen solution samples had 46% $MMOH_Q$, 39.5% $MMOH_{red}$, and 14.5% $MMOH_{ox}$.

The $S = 1$, $Fe^{IV} = O$ complex ($[Fe^{IV}(O)(2PyN2Q)](PF_6)_2$ (2PyN2Q = 1,1-di(pyridin-2-yl)-*N*,*N*-bis(quinolin-2-ylmethyl)methanamine)) was synthesized and isolated following published procedures [44, 68]. Solid samples for XES data collection were prepared in 1.0 mm Al spacers and sealed with 38 µm thick Kapton tape.

The Fe Kβ XES data were collected at beam line ID-26 of the European Synchrotron Radiation Facility (ESRF) operating at 6 GeV and 200 mA. All samples were measured in a liquid helium cryostat operating at 20 K. The energy of the incident beam was selected using either a Si(111) or Si(311) double crystal monochromator, each of which was calibrated by setting the first inflection of an iron foil to 7111.2 eV. The incident monochromator was then set to an excitation energy of 7800 eV to non-resonantly excite the sample. The XES spectra were collected with a 1 m radius Johann spectrometer equipped with five Ge(620) spherically bent analyzer crystals and calibrated by the scanning of elastic scattering lines. A collected reference Kβ XES spectrum of Fe_2O_3 is displayed in Fig. S1. The measured resolution of the elastic scattering line was ~ 1.5 eV (fwhm) which includes the contribution of the upstream Si(111) monochromator. For the synthetic solid sample, an avalanche photodiode (APD) detector was used, while the more dilute protein samples required the use of an energy resolving Ketek detector to further improve the S/N of the emission spectra. For the XES collection of the protein, the incident beam was attenuated to a maximum estimated flux of 4×10^{12} photons/s within a spot size of 1.2 mm (w) × 0.1 mm (v) to further reduce radiation damage. Maximum sample exposure dwell times were determined through the evaluation of repeated fast X-ray near edge absorption (XANES) scans (5–60 s) to determine total acceptable photon doses [24]. Collection of the protein XES was completed in small segments (~ 12 eV wide, 50–61 points) of the entire XES spectra (7.025–7.08 keV) with 2 eV overlap per energy segment (10–11 data points). Each segment was collected on a fresh sample spot, limiting the total sample spot exposure time. The maximum dwell times per data point were: $MMOH_{red}$, 1.25 secs; $MMOH_{ox}$ 0.40 secs; $MMOH_Q$, 0.15 secs. This limited the sample spot exposure times to a maximum of 76.25 secs ($MMOH_{red}$), 24.4 secs ($MMOH_{ox}$) and 15.25 secs ($MMOH_Q$). This collection process allowed for improved signal-to-noise to be acquired at each data point, and to mitigate beam induced damage. All data segments were splined together through the averaging of their overlapping components. A sample of the process is shown in Fig. S2.

All Kβ XES spectra were normalized to a unit area of 1 over the energy range of 7025 to 7080 eV. The XES spectrum of pure $MMOH_Q$ was calculated by subtracting the $MMOH_{red}$ and $MMOH_{ox}$ components from MMOH-RFQ at the ratios determined by Mössbauer and renormalizing to a unit area of 1. The first moments reported are determined over the described energy ranges by the following equation,

$$M_1 = \frac{\sum_i (E_i I_i)}{\sum_i I_i}$$

where E_i and I_i are the energy and intensities, respectively, at data point i.

Results

Samples of $MMOH_{red}$, $MMOH_{ox}$ and rapid-freeze-quenched (RFQ) samples of $MMOH_Q$ were prepared as previously described [24]. The Fe Kβ XES spectra of the three prepared

samples of sMMO ($MMOH_{red/ox/RFQ}$) are shown in Fig. 2a. No significant differences in the $K\beta_{1,3}$ maxima are apparent. One does, however, observe slight intensity differences in the Kβ' region (at ~ 7045 eV) following a trend of $MMOH_{red} > MMOH_{ox} > MMOH\text{-}RFQ$. As the RFQ sample is a mixture of all three different components and therefore three oxidation states, an assignment of the convoluted spectrum is challenging. The individual components of the RFQ samples were quantitated by ^{57}Fe Mössbauer spectroscopy, with an estimated 46% yield of $MMOH_Q$ [24]. The ^{57}Fe Mössbauer quantification of each component in the MMOH-RFQ sample allows for the 'pure' $MMOH_Q$ spectrum to be calculated as previously established in the HERFD XAS studies of sMMO and other non-heme di-iron proteins [23, 69].

The 'pure' $MMOH_Q$ mainline spectrum is shown in Fig. 2b, overlaid with $MMOH_{red}$ and $MMOH_{ox}$. Here, one can clearly see that the $K\beta_{1,3}$ peak position does not shift for the various oxidation states $Fe^{II}_2/Fe^{III}_2/Fe^{IV}_2$ of sMMO. Often, the first moment of the $K\beta_{1,3}$ is used rather than the peak maximum to determine energy shifts because the first moment has been shown to have more sensitivity to small changes [54, 70–72]. However, the first moment analysis of the three spectra, Table 2, does not reveal significant energy shifts either, even though it was previously shown that all three of these samples exhibit clearly different XAS pre-edge and rising edge energies (see Figure S5 in Ref. [24]), consistent with their anticipated oxidation states and previous HERFD-XAS characterization [23].

While the $K\beta_{1,3}$ may not exhibit clear differences with oxidation-state changes, the Kβ' intensity of the three states clearly varies, Fig. 2b. The Kβ' feature of $MMOH_{red}$ appears slightly more intense than $MMOH_{ox}$. This is in agreement with the subtle intensity differences observed in other high-spin Fe^{II} versus Fe^{III} mainlines, such as $[Fe(H_2O)_6]^{2+/3+}$ [58]. $MMOH_Q$ has a clear Kβ' feature, indicating that there are unpaired d electrons ($S_{loc} > 0$). The first moment of the Kβ' of $MMOH_Q$ feature is at approximately the same energy as the more reduced iron species. In fact, the Kβ' features for each of the three MMOH states appear at approximately the same energies, with only the intensities of the Kβ' features varying, making the $\Delta(K\beta_{1,3} - K\beta')$ splitting approximately the same for each species, Table 2.

The mainline of $MMOH_Q$ may be the result of two local Fe^{IV} spin states: high-spin $S = 2$, or intermediate-spin $S = 1$. To determine the spin state, the mainline is directly compared to the Fe^{IV} $S = 1$ mainline from an $Fe^{IV} = O$ complex $[Fe(O)2PyN2Q)]^{2+}$, Scheme 1. Two immediate

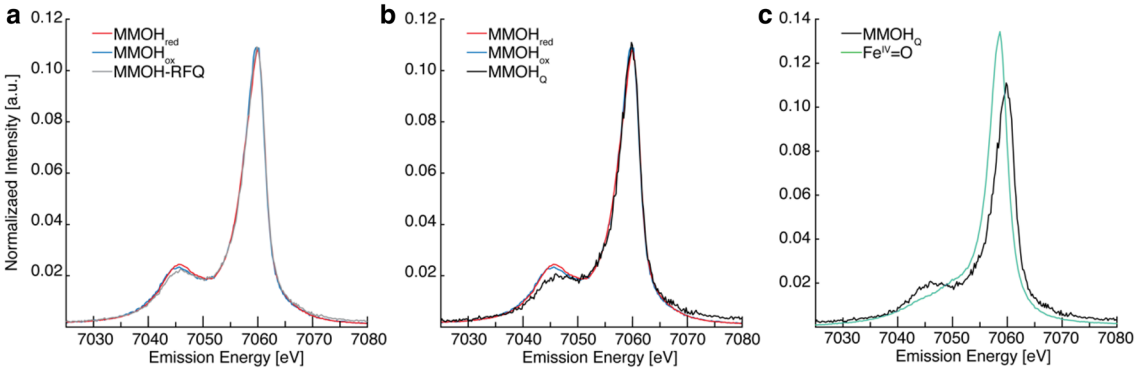

Fig. 2 **a** Fe Kβ mainline XES of $MMOH_{red}$, $MMOH_{ox}$ and MMOH-RFQ samples of sMMO. **b** The $MMOH_Q$ spectrum is determined by subtraction of the $MMOH_{red}$ and $MMOH_{ox}$ components from the MMOH-RFQ spectrum. **c** The $MMOH_Q$ XES is compared to that of an $S = 1$ $Fe^{IV} = O$

Table 2 Key Fe Kβ mainline parameters

	Kβ First Moment[a]	$K\beta_{1,3}$ First Moment[b]	Kβ' First Moment[c]	$\Delta(K\beta_{1,3}–K\beta')$
$MMOH_{red}$	7054.94	7058.96	7043.59	15.37
$MMOH_{ox}$	7055.00	7059.00	7043.75	15.25
RFQ	7055.20	7059.05	7043.59	15.46
$MMOH_Q$	7055.45	7059.12	7043.43	15.69
$Fe(IV) = O$	7055.38	7058.16	7044.10	14.06

All values have energy units of eV

[a]Determined over entire measured Kβ mainline spectrum, 7025–7080 eV

[b]Determined over the energy range of 7051–7070 eV

[c]Determined over the energy range of 7025–7051 eV

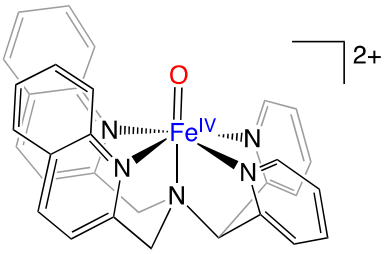

Scheme 1 $Fe^{IV}=O$; $[Fe(O)(2PyN2Q)]^{2+}$

differences are observed in the spectra plotted in Fig. 2c. First, the $K\beta_{1,3}$ energy for the $Fe^{IV}=O$ $S=1$ model complex is clearly shifted to lower energy by approximately 1 eV compared to $MMOH_Q$ and second, the Kβ' region for the $Fe^{IV}=O$ model is significantly less intense than that of $MMOH_Q$. Furthermore, the same first moment analysis of the Kβ' of the $Fe^{IV}=O$ mainline reveals an + 1 eV compared to $MMOH_Q$, decreasing the $\Delta(K\beta_{1,3}-K\beta')$ splitting by ~ 2 eV, comparatively.

With respect to the Kβ' intensity of $MMOH_Q$, one may refer to the fingerprinting analyses performed for ferrous ion sites [57–60]. The presence of the Kβ' in the high-spin $S=2$ and its absence in low-spin S = 0 centers is used as a spin-state diagnostic tool. For $MMOH_Q$, the clearly greater intensity of its Kβ' feature and larger $\Delta(K\beta_{1,3}-K\beta')$ splitting compared to that of the established $S=1$ $Fe^{IV}=O$ in Fig. 2c strongly suggests *higher* local spin states for the Fe^{IV} ions of $MMOH_Q$.

For the $\Delta(K\beta_{1,3}-K\beta')$ splitting, it has been previously demonstrated that the energetic splitting is proportional to the nominal spin of the metal center, but these energy shifts may be further modulated by covalency [56]. However, the quantification of the covalency in the various states of MMOH is difficult to estimate. One may naturally consider a potential di-iron(IV) open core structure that contains terminal oxos to be more covalent than the $MMOH_{ox}$ and $MMOH_{red}$ states. However, the previous Mn Kβ mainline characterization of the step-wise deprotonation of high-spin Mn^{IV} $S=2$ $Mn_2(\mu\text{-}OH)_2$ dimers to the $Mn_2(\mu\text{-}O)$ cores exhibited only minimal shifts (~ 0.5 eV) in the $K\beta_{1,3}$ energies [64]. This suggests that when comparing potential oxo vs hydroxo ligation to the iron sites, the covalency changes will result in only minor energetic perturbations and that local iron spin state should be the dominant contribution to the Kβ mainline energies. Our analysis and comparison of the sMMO Kβ mainline lines clearly supports the conclusion that the local spin states of the iron sites of $MMOH_Q$ are $S=2$. Furthermore, the Kβ mainline analysis of $MMOH_Q$ as an $S_{loc}=2$ is very consistent with the $S_{loc}=2$ and $S_{loc}=5/2$ spin states of the $MMOH_{red}$ and $MMOH_{ox}$, respectively [13, 73].

Discussion

While previous Mössbauer experiments of $MMOH_Q$ provide evidence for isomer shifts in clear agreement with Fe^{IV} ions, the antiferromagnetic coupling and $S_{tot}=0$ cluster spin state do not yield conclusive information of the local spin states of the iron sites. Here, we have used Fe Kβ XES to probe the local spin state of $MMOH_Q$. The ΔKβ splitting and the Kβ' intensity of $MMOH_Q$ are excellent indicators of local high-spin $S=2$ iron sites that antiferromagnetically couple to form the $S_{tot}=0$ cluster.

The Kβ mainline of $MMOH_Q$ has distinct features that also resemble other assigned $S=2$ Fe^{IV} centers [58, 74]. In a recent study of the Fe Kβ signatures of various compounds, the Kβ emission spectra of the iron perovskites $LaFe^{III}O_3$ and $SrFe^{IV}O_3$ were reported [58]. In $LaFe^{III}O_3$, a typical $S=5/2$ ferric mainline is observed, whereas the high-spin $S=2$ Fe^{IV} mainline of $SrFe^{IV}O_3$ exhibits a similar $K\beta_{1,3}$ mainline maxima, but a slightly decreased Kβ' intensity, similar to that observed for $MMOH_Q$. However, we do note that this perovskite sample does not have the same molecular and/or electronic properties as the non-heme carboxylate-bridged di-iron center of sMMO, and so only qualitative comparisons are made.

Perhaps the most closely related structure to $MMOH_Q$ is an RNR intermediate. The more widely studied di-iron RNR forms a high-valent Fe^{III}–Fe^{IV} intermediate termed 'X,' that has a $S_{tot}=1/2$ cluster spin state as described earlier. Similarly, the hetero-metallic Mn–Fe class I-c of RNRs also forms a high-valent intermediate Mn^{IV}–Fe^{IV} intermediate [75]. For the d^4 Fe center of the Mn^{IV}–Fe^{IV} RNR, the Fe Kβ mainline does not exhibit any clear energy shifts of the $K\beta_{1,3}$ for the local Fe^{II}, Fe^{III} and Fe^{IV} centers, and the Fe^{IV} Kβ' exhibits a decreased intensity relative to the lower Fe oxidation-state intermediates [74]. The Fe Kβ XES of the $S=2$ Fe^{IV} center from Mn–Fe RNR has similar intensity to what we have observed for $MMOH_Q$ (Figs. S3 and S4), lending additional support to the idea that measured Kβ XES of $MMOH_Q$ reflects two $S=2$ Fe^{IV} ions and not a beam damaged product yielding high-spin $S=5/2$ ferric sites, which would further increase Kβ' intensity and ΔKβ splitting.[25, 50] Furthermore, the ΔKβ splitting observed in RNR is similar to that seen here in $MMOH_Q$, Fig. S4. It is important again to note the clear presence of a Kβ' feature in the $S=2$ Fe^{IV} RNR compared to the lack of a well-resolved Kβ' in the $S=1$ $Fe^{IV}=O$ model reported here (Fig. S4), offering further support that that the Kβ mainline observed for $MMOH_Q$ is diagnostic of an $S=2$ local spin states at the iron atoms.

Conclusion and outlook

In summary, the high-spin Fe^{II}, Fe^{III} and Fe^{IV} sites of sMMO do not exhibit oxidation-state-dependent energy shifts by Fe Kβ XES. Modest differences are observed in the Kβ' due to spin state. Notably, the ΔKβ($Kβ_{1,3}$-Kβ') splitting of sMMO remains fairly constant, which is very consistent with high-spin states for $MMOH_{ox}$, $MMOH_{red}$, and $MMOH_Q$. Direct comparison of the $MMOH_Q$ mainline to a known $S = 1$ Fe^{IV} complex has shown dramatic spectral differences due to changes in the apparent spin state. This approach, in line with Fe Kβ XES spin state fingerprinting for ferrous and ferric iron, clearly distinguishes between the intermediate $S = 1$ spin of the model complex studied here and the apparent $S_{loc} = 2$ of $MMOH_Q$. The Kβ XES experiment offers a clear experimental approach to determine local spin state in ambiguous systems, where magnetic spin coupling may make such determinations challenging for other experimental methods.

In the realm of X-ray spectroscopic studies, XES has become a viable tool to monitor spin state and/or oxidation states in both static samples and in situ or operando studies. Some of the clearest utility of Fe Kβ XES has been to discriminate between low- versus high-spin iron species [56–60]. The lack of significant shifts in $Kβ_{1,3}$ mainline energies for the different oxidation states of MMOH intermediates precludes one from attempting more advanced X-ray spectroscopic techniques, such as "site selective" XAS or EXAFS for further enhancement of the $MMOH_Q$ signal in the mixed sample through the means of energy selective detection [76, 77]. The mainline spectra reported here will be valuable in future studies of sMMO. With the previous success of using Mn Kβ emission to fingerprint oxidation state during in situ measurements [70, 78], one hopes to be able to utilize the Fe Kβ XES to fingerprint, monitor and validate electronic changes during in situ studies. Such XES approaches have been highlighted in X-ray free electron laser (XFEL) protein diffraction studies to monitor a catalytic site's oxidation-state [79, 80]. The present results on the Fe Kβ mainlines of sMMO, however, demonstrate the potential difficulty of employing such methods for monitoring oxidation-state during in situ studies, where the $Kβ_{1,3}$ energy does not offer great sensitivity but the Kβ' itself offers spin state (correlated to the oxidation-state) information through its clear intensity changes. Given the inherently lower intensity of the Kβ' feature, using this feature to follow spin state will require data collection with high signal-to-noise to ensure accurate assignments. We do note that the Kα ($2p \rightarrow 1s$) emission spectrum is an order of magnitude more intense than the Kβ emission, allowing for easier measurements. Kα XES does not offer the same degree of electronic sensitivity, and extraction of oxidation or spin-state information is challenging [54, 58]. The three states of sMMO do not exhibit significant energy differences in their Kα spectra (Figure S6 in ref [24].) and more recent Kα XES of $MMOH_{red}$ and $MMOH_{ox}$ collected during XFEL crystallography experiments exhibits only subtle changes in the linewidths and shapes [81]. While more challenging to collect, Kβ XES appears to offer the most sensitivity to spin state and the best potential fingerprint for formation of the di-iron(IV) ($S_{loc} = 2$) cluster.

Fe Kβ XES of sMMO has proven to be a valuable technique to probe the local spin states of the di-iron site in the catalytic cluster. Understanding and verifying that $MMOH_Q$ is, in fact, $S_{loc} = 2$ is important to both understanding and proposing mechanisms for reactivity. Further, the ability to clearly distinguish $S = 1$ from $S = 2$ iron sites via Kβ XES has potential for experimentally assessing the role of two-state reactivity in a wide range of high-valent Fe^{IV}–oxo complexes [48, 82]. Hence, the present results deepen our understanding of the electronic structure of $MMOH_Q$, while providing experimental fingerprints to enable the study of a wide range of high-valent iron species in both molecular models and enzymes.

Supplementary Information The online version contains supplementary material available at https://doi.org/10.1007/s00775-022-01953-4.

Acknowledgements Various members of the Inorganic Spectroscopy Department at the MPI CEC are thanked for helpful assistance with X-ray data collection. Bernd Meinert (MPI KoFo) is thanked for assistance in Mössbauer data collection. Financial support was provided by the Max Planck Society and the International Max Planck Research School (IMPRS) Recharge. J.D.L. acknowledge the National Institutes of Health for funding (GM118030). The XES experiments were performed on beamline ID-26 at the European Synchrotron Radiation Facility (ESRF), Grenoble, France. We are grateful to Dr. Blanka Detlefs, Dr. Lucia Amidani and Dr. Pieter Glatzel at the ESRF for providing assistance in using beamline ID-26.

Funding Open Access funding enabled and organized by Projekt DEAL.

Data availability The datasets generated during and/or analyzed during the current study are available from the corresponding author on reasonable request.

Declarations

Conflict of interest The authors have no competing interests to declare that are relevant to the content of this article.

References

1. Hanson RS, Hanson TE (1996) Microbiol Rev 60:439–471. https://doi.org/10.1128/mr.60.2.439-471.1996
2. Ross MO, Rosenzweig AC (2017) J Biol Inorg Chem 22:307–319. https://doi.org/10.1007/s00775-016-1419-y
3. Sirajuddin S, Rosenzweig AC (2015) Biochemistry 54:2283–2294. https://doi.org/10.1021/acs.biochem.5b00198
4. Culpepper MA, Rosenzweig AC (2012) Crit Rev Biochem Mol 47:483–492. https://doi.org/10.3109/10409238.2012.697865
5. Cutsail GE III, Ross MO, Rosenzweig AC, DeBeer S (2021) Chem Sci 12:6194–6209. https://doi.org/10.1039/d1sc00676b
6. Jodts RJ, Ross MO, Koo CW, Doan PE, Rosenzweig AC, Hoffman BM (2021) J Am Chem Soc 143:15358–15368. https://doi.org/10.1021/jacs.1c07018
7. Peng W, Qu XY, Shaik S, Wang BJ (2021) Nat Catal 4:266–273. https://doi.org/10.1038/s41929-021-00591-4
8. Ross MO, MacMillan F, Wang J, Nisthal A, Lawton TJ, Olafson BD, Mayo SL, Rosenzweig AC, Hoffman BM (2019) Science 364:566–570. https://doi.org/10.1126/science.aav2572
9. Ro SY, Schachner LF, Koo CW, Purohit R, Remis JP, Kenney GE, Liauw BW, Thomas PM, Patrie SM, Kelleher NL, Rosenzweig AC (2019) Nat Commun 10:2675. https://doi.org/10.1038/s41467-019-10590-6
10. Chang WH, Lin HH, Tsai IK, Huang SH, Chung SC, Tu IP, Yu SS, Chan SI (2021) J Am Chem Soc 143:9922–9932. https://doi.org/10.1021/jacs.1c04082
11. Christopher WK, Frank JT, He Y, Amy CR (2022) Science 375:1287–1291. https://doi.org/10.1126/science.abm3282
12. Stanley SH, Prior SD, Leak DJ, Dalton H (1983) Biotechnol Lett 5:487–492. https://doi.org/10.1007/Bf00132233
13. Fox BG, Hendrich MP, Surerus KK, Andersson KK, Froland WA, Lipscomb JD, Münck E (1993) J Am Chem Soc 115:3688–3701. https://doi.org/10.1021/ja00062a039
14. Wallar BJ, Lipscomb JD (1996) Chem Rev 96:2625–2658. https://doi.org/10.1021/cr9500489
15. Liu KE, Wang DL, Huynh BH, Edmondson DE, Salifoglou A, Lippard SJ (1994) J Am Chem Soc 116:7465–7466. https://doi.org/10.1021/ja00095a083
16. Liu KE, Valentine AM, Wang DL, Huynh BH, Edmondson DE, Salifoglou A, Lippard SJ (1995) J Am Chem Soc 117:10174–10185. https://doi.org/10.1021/ja00146a002
17. Tinberg CE, Lippard SJ (2011) Acc Chem Res 44:280–288. https://doi.org/10.1021/ar1001473
18. Shu L, Nesheim JC, Kauffmann K, Münck E, Lipscomb JD, Que L Jr (1997) Science 275:515–518. https://doi.org/10.1126/science.275.5299.515
19. Lee SK, Nesheim JC, Lipscomb JD (1993) J Biol Chem 268:21569–21577. https://doi.org/10.1016/S0021-9258(20)80579-1
20. Lee SK, Fox BG, Froland WA, Lipscomb JD, Münck E (1993) J Am Chem Soc 115:6450–6451. https://doi.org/10.1021/ja00067a086
21. Banerjee R, Proshlyakov Y, Lipscomb JD, Proshlyakov DA (2015) Nature 518:431–434. https://doi.org/10.1038/nature14160
22. Banerjee R, Meier KK, Münck E, Lipscomb JD (2013) Biochemistry 52:4331–4342. https://doi.org/10.1021/bi400182y
23. Castillo RG, Banerjee R, Allpress CJ, Rohde GT, Bill E, Que L Jr, Lipscomb JD, DeBeer S (2017) J Am Chem Soc 139:18024–18033. https://doi.org/10.1021/jacs.7b09560
24. Cutsail GE III, Banerjee R, Zhou A, Que L Jr, Lipscomb JD, DeBeer S (2018) J Am Chem Soc 140:16807–16820. https://doi.org/10.1021/jacs.8b10313
25. Jacobs AB, Banerjee R, Deweese DE, Braun A, Babicz JT, Gee LB, Sutherlin KD, Bottger LH, Yoda Y, Saito M, Kitao S, Kobayashi Y, Seto M, Tamasaku K, Lipscomb JD, Park K, Solomon EI (2021) J Am Chem Soc 143:16007–16029. https://doi.org/10.1021/jacs.1c05436
26. Banerjee R, Jones JC, Lipscomb JD (2019) Ann Rev Biochem 88:409–431. https://doi.org/10.1146/annurev-biochem-013118-111529
27. Rosenzweig AC (2015) Nature 518:309–310. https://doi.org/10.1038/nature14199
28. Whittington DA, Lippard SJ (2001) J Am Chem Soc 123:827–838. https://doi.org/10.1021/ja003240n
29. Schulz CE, Castillo RG, Pantazis DA, DeBeer S, Neese F (2021) J Am Chem Soc 143:6560–6577. https://doi.org/10.1021/jacs.1c01180
30. Que L Jr (2007) Acc Chem Res 40:493–500. https://doi.org/10.1021/ar700024g
31. Krebs C, Fujimori DG, Walsh CT, Bollinger JM Jr (2007) Acc Chem Res 40:484–492. https://doi.org/10.1021/ar700066p
32. Sinnecker S, Svensen N, Barr EW, Ye S, Bollinger JM Jr, Neese F, Krebs C (2007) J Am Chem Soc 129:6168–6179. https://doi.org/10.1021/ja067899q
33. Jasniewski AJ, Que L Jr (2018) Chem Rev 118:2554–2592. https://doi.org/10.1021/acs.chemrev.7b00457
34. Que L Jr, Tolman WB (2008) Nature 455:333–340. https://doi.org/10.1038/nature07371
35. Sturgeon BE, Burdi D, Chen SX, Huynh BH, Edmondson DE, Stubbe J, Hoffman BM (1996) J Am Chem Soc 118:7551–7557. https://doi.org/10.1021/ja960399k
36. Xue G, Wang D, De Hont R, Fiedler AT, Shan X, Münck E, Que L Jr (2007) Proc Natl Acad Sci USA 104:20713–20718. https://doi.org/10.1073/pnas.0708516105
37. Xue GQ, Fiedler AT, Martinho M, Münck E, Que L Jr (2008) Proc Natl Acad Sci USA 105:20615–20620. https://doi.org/10.1073/pnas.0808512105
38. Puri M, Que L Jr (2015) Acc Chem Res 48:2443–2452. https://doi.org/10.1021/acs.accounts.5b00244
39. Stoian SA, Xue G, Bominaar EL, Que L Jr, Münck E (2014) J Am Chem Soc 136:1545–1558. https://doi.org/10.1021/ja411376u
40. Riggs-Gelasco PJ, Price JC, Guyer RB, Brehm JH, Barr EW, Bollinger JM Jr, Krebs C (2004) J Am Chem Soc 126:8108–8109. https://doi.org/10.1021/ja048255q
41. Martinho M, Xue G, Fiedler AT, Que L Jr, Bominaar EL, Münck E (2009) J Am Chem Soc 131:5823–5830. https://doi.org/10.1021/ja8098917
42. Rohde JU, In JH, Lim MH, Brennessel WW, Bukowski MR, Stubna A, Münck E, Nam W, Que L Jr (2003) Science 299:1037–1039. https://doi.org/10.1126/science.299.5609.1037
43. Klinker EJ, Kaizer J, Brennessel WW, Woodrum NL, Cramer CJ, Que L Jr (2005) Angew Chem Int Ed 44:3690–3694. https://doi.org/10.1002/anie.200500485
44. Rasheed W, Draksharapu A, Banerjee S, Young VG, Fan R, Guo Y, Ozerov M, Nehrkorn J, Krzystek J, Telser J, Que L Jr (2018) Angew Chem Int Ed 57:9387–9391. https://doi.org/10.1002/anie.201804836

45. England J, Martinho M, Farquhar ER, Frisch JR, Bominaar EL, Münck E, Que L Jr (2009) Angew Chem Int Ed 48:3622–3626. https://doi.org/10.1002/anie.200900863
46. Warm K, Paskin A, Kuhlmann U, Bill E, Swart M, Haumann M, Dau H, Hildebrandt P, Ray K (2021) Angew Chem Int Ed 60:6752–6756. https://doi.org/10.1002/anie.202015896
47. Pestovsky O, Stoian S, Bominaar EL, Shan XP, Münck E, Que L Jr, Bakac A (2005) Angew Chem Int Ed 44:6871–6874. https://doi.org/10.1002/anie.200502686
48. Swart M, Costas M (2016) Spin states in biochemistry and inorganic chemistry. John Wiley and Sons Ltd., West Sussex
49. Xue G, De Hont R, Münck E, Que L Jr (2010) Nat Chem 2:400–405. https://doi.org/10.1038/nchem.586
50. Valentine AM, Tavares P, Pereira AS, Davydov R, Krebs C, Hoffman BM, Edmondson DE, Huynh BH, Lippard SJ (1998) J Am Chem Soc 120:2190–2191. https://doi.org/10.1021/ja974169x
51. Gherman BF, Dunietz BD, Whittington DA, Lippard SJ, Friesner RA (2001) J Am Chem Soc 123:3836–3837. https://doi.org/10.1021/ja0055108
52. Siegbahn PEM (1999) Inorg Chem 38:2880–2889. https://doi.org/10.1021/ic981332w
53. Han W-G, Noodleman L (2008) Inorg Chim Acta 361:973–986. https://doi.org/10.1016/j.ica.2007.06.007
54. Glatzel P, Bergmann U (2005) Coord Chem Rev 249:65–95. https://doi.org/10.1016/j.ccr.2004.04.011
55. Castillo RG, Hahn AW, Van Kuiken BE, Henthorn JT, McGale J, DeBeer S (2021) Angew Chem Int Ed 60:10112–10121. https://doi.org/10.1002/anie.202015669
56. Pollock CJ, Delgado-Jaime MU, Atanasov M, Neese F, DeBeer S (2014) J Am Chem Soc 136:9453–9463. https://doi.org/10.1021/ja504182n
57. Lee N, Petrenko T, Bergmann U, Neese F, DeBeer S (2010) J Am Chem Soc 132:9715–9727. https://doi.org/10.1021/ja101281e
58. Lafuerza S, Carlantuono A, Retegan M, Glatzel P (2020) Inorg Chem 59:12518–12535. https://doi.org/10.1021/acs.inorgchem.0c01620
59. Mara MW, Hadt RG, Reinhard ME, Kroll T, Lim H, Hartsock RW, Alonso-Mori R, Chollet M, Glownia JM, Nelson S, Sokaras D, Kunnus K, Hodgson KO, Hedman B, Bergmann U, Gaffney KJ, Solomon EI (2017) Science 356:1276–1280. https://doi.org/10.1126/science.aam6203
60. Schuth N, Mebs S, Huwald D, Wrzolek P, Schwalbe M, Hemschemeier A, Haumann M (2017) Proc Natl Acad Sci USA 114:8556–8561. https://doi.org/10.1073/pnas.1706527114
61. Kowalska JK, Lima FA, Pollock CJ, Rees JA, DeBeer S (2016) Isr J Chem 56:803–815. https://doi.org/10.1002/ijch.201600037
62. Peng G, Degroot FMF, Hamalainen K, Moore JA, Wang X, Grush MM, Hastings JB, Siddons DP, Armstrong WH, Mullins OC, Cramer SP (1994) J Am Chem Soc 116:2914–2920. https://doi.org/10.1021/ja00086a024
63. Kowalska JK, Hahn AW, Albers A, Schiewer CE, Bjornsson R, Lima FA, Meyer F, DeBeer S (2016) Inorg Chem 55:4485–4497. https://doi.org/10.1021/acs.inorgchem.6b00295
64. Lassalle-Kaiser B, Boron TT, Krewald V, Kern J, Beckwith MA, Delgado-Jaime MU, Schroeder H, Alonso-Mori R, Nordlund D, Weng T-C, Sokaras D, Neese F, Bergmann U, Yachandra VK, DeBeer S, Pecoraro VL, Yano J (2013) Inorg Chem 52:12915–12922. https://doi.org/10.1021/ic400821g
65. Rees JA, Bjornsson R, Kowalska JK, Lima FA, Schlesier J, Sippel D, Weyhermüller T, Einsle O, Kovacs JA, DeBeer S (2017) Dalton Trans 46:2445–2455. https://doi.org/10.1039/C7DT00128B
66. Lambertz C, Chernev P, Klingan K, Leidel N, Sigfridsson KGV, Happe T, Haumann M (2014) Chem Sci 5:1187–1203. https://doi.org/10.1039/C3SC52703D
67. Banerjee R, Komor AJ, Lipscomb JD (2017) Methods Enzymol 596:239–290. https://doi.org/10.1016/bs.mie.2017.07.016
68. Massie AA, Denler MC, Cardoso LT, Walker AN, Hossain MK, Day VW, Nordlander E, Jackson TA (2017) Angew Chem Int Ed 56:4178–4182. https://doi.org/10.1002/anie.201612309
69. Cutsail GE III, Blaesi EJ, Pollock CJ, Bollinger JM Jr, Krebs C, DeBeer S (2020). J Inorg Biochem. https://doi.org/10.1016/j.jinorgbio.2019.110877
70. Fransson T, Chatterjee R, Fuller FD, Gul S, Weninger C, Sokaras D, Kroll T, Alonso-Mori R, Bergmann U, Kern J, Yachandra VK, Yano J (2018) Biochemistry 57:4629–4637. https://doi.org/10.1021/acs.biochem.8b00325
71. Eeckhout SG, Safonova OV, Smolentsev G, Biasioli M, Safonov VA, Vykhodtseva LN, Sikora M, Glatzel P (2009) J Anal Atom Spectr 24:215–223. https://doi.org/10.1039/B808345M
72. Jensen SC, Davis KM, Sullivan B, Hartzler DA, Seidler GT, Casa DM, Kasman E, Colmer HE, Massie AA, Jackson TA, Pushkar Y (2017) J Phys Chem Lett 8:2584–2589. https://doi.org/10.1021/acs.jpclett.7b01209
73. Hendrich MP, Münck E, Fox BG, Lipscomb JD (1990) J Am Chem Soc 112:5861–5865. https://doi.org/10.1021/ja00171a029
74. Martinie RJ, Blaesi EJ, Krebs C, Bollinger JM Jr, Silakov A, Pollock CJ (2017) J Am Chem Soc 139:1950–1957. https://doi.org/10.1021/jacs.6b11563
75. Jiang W, Hoffart LM, Krebs C, Bollinger JM Jr (2007) Biochemistry 46:8709–8716. https://doi.org/10.1021/bi700906g
76. Glatzel P, Jacquamet L, Bergmann U, de Groot FM, Cramer SP (2002) Inorg Chem 41:3121–3127. https://doi.org/10.1021/ic010709m
77. de Groot FMF (2000) Top Catal 10:179–186. https://doi.org/10.1023/a:1019140823425
78. Ibrahim M, Fransson T, Chatterjee R, Cheah MH, Hussein R, Lassalle L, Sutherlin KD, Young ID, Fuller FD, Gul S, Kim IS, Simon PS, de Lichtenberg C, Chernev P, Bogacz I, Pham CC, Orville AM, Saichek N, Northen T, Batyuk A, Carbajo S, Alonso-Mori R, Tono K, Owada S, Bhowmick A, Bolotovsky R, Mendez D, Moriarty NW, Holton JM, Dobbek H, Brewster AS, Adams PD, Sauter NK, Bergmann U, Zouni A, Messinger J, Kern J, Yachandra VK, Yano J (2020) Proc Natl Acad Sci USA 117:12624–12635. https://doi.org/10.1073/pnas.2000529117
79. Bergmann U, Kern J, Schoenlein RW, Wernet P, Yachandra VK, Yano J (2021) Nat Phys Rev 3:264–282. https://doi.org/10.1038/s42254-021-00289-3
80. Kern J, Alonso-Mori R, Tran R, Hattne J, Gildea RJ, Echols N, Glöckner C, Hellmich J, Laksmono H, Sierra RG, Lassalle-Kaiser B, Koroidov S, Lampe A, Han G, Gul S, DiFiore D, Milathianaki D, Fry AR, Miahnahri A, Schafer DW, Messerschmidt M, Seibert MM, Koglin JE, Sokaras D, Weng T-C, Sellberg J, Latimer MJ, Grosse-Kunstleve RW, Zwart PH, White WE, Glatzel P, Adams PD, Bogan MJ, Williams GJ, Boutet S, Messinger J, Zouni A, Sauter NK, Yachandra VK, Bergmann U, Yano J (2013) Science 340:491–495. https://doi.org/10.1126/science.1234273
81. Srinivas V, Banerjee R, Lebrette H, Jones JC, Aurelius O, Kim I-S, Pham CC, Gul S, Sutherlin KD, Bhowmick A, John J, Bozkurt E, Fransson T, Aller P, Butryn A, Bogacz I, Simon P, Keable S, Britz A, Tono K, Kim KS, Park S-Y, Lee SJ, Park J, Alonso-Mori R, Fuller FD, Batyuk A, Brewster AS, Bergmann U, Sauter NK, Orville AM, Yachandra VK, Yano J, Lipscomb JD, Kern J, Högbom M (2020) J Am Chem Soc 142:14249–14266. https://doi.org/10.1021/jacs.0c05613
82. Shaik S (2020) Isr J Chem 60:938–956. https://doi.org/10.1002/ijch.202000002

Authors and Affiliations

George E. Cutsail III[1,2] · Rahul Banerjee[3] · Derek B. Rice[1] · Olivia McCubbin Stepanic[1] · John D. Lipscomb[3] · Serena DeBeer[1]

[1] Max Planck Institute for Chemical Energy Conversion, Stiftstrasse 34-36, 45470 Mülheim an der Ruhr, Germany

[2] Institute of Inorganic Chemistry, University of Duisburg-Essen, Universitätsstrasse 5-7, 45117 Essen, Germany

[3] Department of Biochemistry Molecular Biology and Biophysics, University of Minnesota, Minneapolis, MN 55455, USA